

10/11

10-36

361103

Laser-Induced Incandescence Measurements in Low Gravity

R. L. Vander Wal
Nyma@NASA-Lewis
M.S. 110-3
21,000 Brookpark Rd.
Cleveland, OH 44135

Ph. (216) 433-9065
Fax (216) 433-3793
email: randy@rvander.lerc.nasa.gov

Abstract

A low-gravity environment offers advantages to investigations concerned with soot growth or flame radiation by eliminating of buoyancy-induced convection. Basic to each type of study is knowledge of spatially resolved soot volume fraction, (f_v). Laser-induced incandescence (LII) has emerged as a diagnostic for soot volume fraction determination because it possesses high temporal and spatial resolution, geometric versatility and high sensitivity. Implementation and system characterization of LII in a drop tower that provides 2.2 sec of low-gravity (μg) at the NASA Lewis Research Center are described here. Validation of LII for soot volume fraction determination in μg is performed by comparison between soot volume fraction measurements obtained by light extinction [20] and LII in low-gravity for a 50/50 mixture (by volume) of acetylene/nitrogen issuing into quiescent air. Quantitative soot volume fraction measurements within other laminar flames of ethane and propane and a turbulent diffusion flame in $1-g$ via LII are also demonstrated. An analysis of LII images of a turbulent acetylene diffusion flame in $1-g$ and μg is presented.

Introduction

Determination of soot volume fraction (f_v) is important due to the wide range of combustion processes in which soot is found. In addition to representing incomplete combustion and an unwanted pollutant when emitted from flames, the presence of soot also affects other physical and chemical properties of combustion such as flame temperature and reaction kinetics through radiative heat loss.

The pervasiveness of soot in combustion of hydrocarbon fuels has motivated numerous investigations. Soot formation and growth processes include fuel pyrolysis, PAH formation/growth, particle inception and subsequent surface mass growth [1]. To provide experimental data for testing current soot formation and growth models requires spatially resolving the temperatures and time-scales of these processes [2]. A microgravity environment provides monotonic paths in temperature and mixture fraction for flow trajectories along which soot formation/growth occurs [3]. In the absence of buoyancy-induced convection, spatial and temporal scales are also greatly extended within laminar flames, thereby aiding experimental resolution [4]. Regardless of these extended scales, sensitive and spatially resolved measurements of soot volume fraction must be made. Other studies seek to resolve more subtle effects of buoyancy and radiative heat transfer upon soot processes within rapid time-varying processes such as turbulent flames [5]. High temporal and spatial resolution is required for soot volume fraction measurements in these systems.

A microgravity environment, by eliminating buoyantly driven transport, also facilitates the study of radiation from flames where it is often becomes the dominant energy loss mechanism [6], lowering the flame temperature thereby altering the reaction kinetics [6]. Precombustion processes are also affected by soot radiation. Fuel pyrolysis and vaporization rates are increased by radiative heat transfer due to soot. Since soot contributes substantially to flame radiation, often dominating the gaseous contribution [7], knowledge of soot volume fraction is central to modelling soot

radiation and understanding its consequences for these flame characteristics.

LII has advanced soot volume fraction (f_v) measurements in many 1-g combustion processes. By virtue of its high sensitivity, geometric versatility and temporal capability, LII offers many advantages compared to traditional techniques as demonstrated by application of LII to internal combustion engines [8,9], laminar [10-16] and turbulent gas-jet diffusion flames [14,17], rich premixed flames [11] and droplet combustion [18]. Since the LII signal can be created with a 10 nanosecond duration laser pulse and signal collection in an imaging mode can be achieved within the same timescale, the technique possesses high temporal capability. LII also possesses high spatial resolution, provides 2-D imaging, and offers geometric versatility.

Thus even though LII has been validated against both light extinction and gravimetric sampling in 1-g [10,11,17], verification of LII in μg was desirable. Larger primary particles (50 - 100 % increased radius) and much larger aggregates (by order of magnitude) have been found in μg compared to 1g [19]. Additionally, the temperatures and time scales associated with soot formation/growth processes can also differ dramatically between 1-g and μg [2]. Thus to verify the validity of the LII measurements as representative of f_v in low gravity, LII radial intensity profiles are compared with those derived from a full-field extinction method for a laminar gas-jet flame of 50/50 nitrogen/acetylene (volume/volume) [20]. This comparison of LII and light extinction also tests the viability of the excitation and collection/processing components of the LII measurements in μg . Reported here are the first characterization and demonstrations of LII performed in a low-gravity environment, provided by the NASA Lewis 2.2 sec drop tower facility.

Experimental

In the 2.2 sec drop tower facility at NASA-Lewis, experiments are contained within

packages measuring 41 x 83 x 96 cm (W x L x H) with maximum weight of 159 kg. Release of the package into free-fall yields a low-gravity duration of approximately 2.2 seconds during which peak accelerations of $\sim 10^{-4}$ g are experienced in the absence of cables tethered to the drop rig. Peak shocks of 15 - 30 g occur during 0.2 sec of deceleration. A detailed description is available elsewhere [21].

To enable LII, light from a pulsed Nd:YAG laser (Big Sky Laser Inc.) was delivered via a 35 m long section of high OH-content, 1000 μ m core diameter (30 μ m cladding thickness) optical fiber to the drop package from the stationary laser resident on the top floor of the drop tower. The jacket of the optical fiber consisted of black PVC with Kevlar-strengthening fibers. Laser light at 532 nm from a short cavity, pulsed Nd:YAG laser was coupled into the optical fiber using a 200 mm focal length plano-convex BK-7 lens. A special high power SMA-905 input connector was vital to coupling the pulsed laser light into the optical fiber. The combined coupling and transmission efficiency through the 35 meter optical fiber was roughly 75% efficient.

Figures 1a and 1b illustrate top and side views of the drop rig layout respectively. The divergence of the laser light at 532 nm emerging from the optical fiber is reduced by a 50-mm diameter, 100-mm-focal-length fused silica spherical lens placed approximately 40 mm after the fiber. A sheet is formed using a 125-mm focal length, 50-mm round cylindrical lens. Only the central 30 mm of the light sheet, representing the most uniform intensity, is used for creating the LII images detected by the intensified gated array camera. A dichroic mirror following the cylindrical lens allowed for precise placement of the light sheet through the flame centerline. A beam dump collected the laser light after the burner thereby eliminating scattered laser light. With an incident energy of 10 mJ and estimated beam sheet width of 400 μ m, the laser intensity was roughly 1×10^7 W/cm².

LII images were detected by a ruggedized Xybion ISG-250 ICCD camera through a

bandpass interference filter transmitting 400-450 nm. A glass lens used at f/8 fitted with a 10 mm extension tube provided a field of view of 30 mm. A custom electronics module provided power to the camera from the rig batteries and coupled the video and related timing signals out from the ICCD camera and gate pulse into the camera intensifier. A periscope arrangement relayed the flame image to a CCD (charge coupled device) camera used to collect natural flame emission images for detection of any flame disturbances. The bottom mirror of this periscope is the reflective portion of the bandpass interference filter used to spectrally define the detected LII signal. Natural flame luminosity images were collected by a Sony XC-77 black and white video camera.

Figure 2 illustrates the equipment and signals layout. Video signals from both cameras were transmitted through FM (6MHz bandwidth) video transmitters attached to the drop rig, a dual fiber-optic video cable running between the drop rig and FM video receivers located on the top floor of the drop tower. The LII signal was recorded on a Beta video tape while the natural flame luminosity was recorded on SVHS video tape. A frame-grabber digitized data for subsequent analysis. Synchronization of the laser, camera intensifier gate and camera video signal was achieved using custom electronics to detect the top-of-frame pulse on each video frame and provide a trigger pulse to a delay generator located on the top floor of the drop tower. The delay generator in turn triggered the laser and provided an inverted TTL pulse to serve as the gate pulse for the ICCD camera intensifier. The pulse was delivered through a 35 m length of BNC (RG58) cable connected to the camera control unit aboard the drop rig.

Figure 3 illustrates the relation between the video vertical drive pulses, the interlaced video fields and the laser pulse. In the ICCD camera, each video field is integrated for 33.3 msec and alternating even and odd fields are read out of the camera every 16.6 msec at each vertical drive pulse. As shown in the timing diagram, the odd and even video fields overlap by 16.6 ms. The pairing of successive even and odd fields creates normal interlaced video. The delay generator synchronizes the laser pulse and camera detection gate to occur during the overlapped portion of

the video fields thereby providing an interlaced image (both even and odd horizontal lines containing LII signal).

Drops were initiated by loading a computer program into an onboard data acquisition/control system. This unit also controlled solid state relays to deliver power to the spark ignitor, cameras, and gas solenoid. A 2 s duration preburn about 1 minute prior to the drop ensured fuel within the gas-jet nozzle and confirmation of fuel delivery, ignition, camera gain and image acquisition all working. Upon package release into free-fall, an electrical circuit was opened to provide a rising edge TTL trigger to initiate fuel delivery and ignition.

Laminar gas-jet diffusion flames at atmospheric pressure were established on a 1.5 mm I.D. nozzle with approximately a 30 degree outside edge taper. The burner for the turbulent gas-jet diffusion flame utilized a 0.51 mm I.D. nozzle (length/diameter > 20) with a pilot diffusion flame [22]. In each case a regulator and fine control valve were adjusted using a mass flow meter to deliver a known fuel flow rate. For the laminar gas-jet flames, the volumetric fuel flow of ethane, propane or the 50/50 acetylene/nitrogen mixture was 70 sccm in both 1-g and μ g environments. The associated Reynolds number for each fuel based on cold gas flow were 150, 240 and 90 respectively. For the turbulent acetylene diffusion flame, the acetylene flow through the central gas-jet tube was 1.0 slpm giving a Reynolds number of 4250 while the acetylene flow for the laminar coannular pilot flame was roughly 10 sccm.

Results and Discussion

LII System Response

Figure 4 illustrates the measured system dependence upon LII intensity. To test this dependence, a laminar steady-state gas-jet flame of ethylene was established in 1-g supported on the same 1.1 mm I.D. burner nozzle with a fuel flow rate of 48 sccm. The signal excitation and

detection were setup as if the measurements were being performed in low-gravity. Consequently, the graph represents the results of an end-to-end test of the LII signal detection, transmitting and processing equipment which includes the intensified camera, the video fiber-optic transmitter plus receiver, beta recorder and the frame-grabber used for digitization of the video signal. With a fixed camera intensifier gain typical of that needed for LII μg measurements, the LII intensity reaching the camera was varied by placing calibrated neutral density filters in the detection optical path. Within the resulting digitized LII image, a region-of-interest (ROI) was defined containing 624 pixels within the flame tip where a rather spatially uniform f_v distribution (less than 20% spatial intensity variation) was observed. The average pixel intensity within this region was then calculated for a single LII image. Since the LII intensity incident upon the camera photocathode varied as,

$$\text{Signal}_{(\text{det})} = C * \text{LII} * 10^{(-\text{N.D.})}$$

where C is a constant, a semi-logarithmic plot of $\text{Signal}_{(\text{det.})}$ versus N.D. filter value should be linear provided all subsequent signal processing is linearly dependent upon the LII signal incident upon the camera photocathode. This is observed in Fig. 4. The error bars represent one standard deviation of the ROI average intensity. Even if the curve were nonlinear, it would still provide a calibration curve for translating final digitized pixel intensities into relative LII intensities. The observed relationship allows straightforward interpretation of relative signal levels as linearly related to LII intensities. As discussed in the LII validation section, the LII intensities can be directly interpreted as proportional to f_v .

Camera gain calibration

Lower LII signals arising from lower soot concentrations could be readily detected by increasing the camera intensifier gain. To establish the relative detection sensitivities at different intensifier gains, calibration measurements were performed. Again, the entire LII

excitation/detection system was set up as if to perform low-gravity measurements. LII images of a laminar steady-state flame of ethylene (48 sccm flow rate) were acquired using different intensifier gains. Neutral density filters maintained the signal intensity within the dynamic range of the detection system. Analysis of a ROI (624 pixels) near the tip of the flame provided an average LII intensity for the particular gain setting. Comparison of the relative LII intensities corrected for the neutral density filter attenuation provided a relative measure of the detection sensitivity at the different gain settings (higher intensifier gains correspond to smaller readout settings). To facilitate comparison, the relative values were normalized by the LII average intensity measured with the lowest practical gain setting. These results are shown in Fig. 5. The error bars were calculated assuming Poisson statistics with the standard deviation calculated as the square root of the average LII pixel intensity. These limits were found empirically to well encompass the variation observed in the average LII intensity calculated within the ROI.

Although the semi-logarithmic plot conveniently illustrates the range of detection sensitivities, there is a physical basis for this method of plotting. Because the photon detection event is described by a Poisson distribution [23] and the intensifier amplification process is exponential [24], with a linear detection system, the detected signal intensity would be expected to scale exponentially with the intensifier gain provided no saturation of the electron multiplication process occurred within the microchannel plate, coupled phosphor screen or CCD pixel well. As Fig. 5 shows, using the intensifier, more than a 1000-fold increase in detection sensitivity can be achieved relative to that at a gain setting of 4.70. Based on soot volume fractions of around 15 ppm for the laminar acetylene/nitrogen (50/50) mixture in 1-g detected using a gain of 4.70, Fig. 5 predicts a detection sensitivity of nearly 0.02 ppm.

LII Validation

To verify the LII measurements as representative of f_v in low gravity, LII radial intensity profiles are compared with those derived from a full-field extinction method for a laminar gas-jet

flame of 50/50 nitrogen/acetylene. The light extinction results have been reported previously [20]. The axial positions were chosen to illustrate different spatial and intensity variations in f_v . Single pixel-wide radial rows of the LII image were selected yielding a spatial resolution of about 80 μm . Each LII profile was also corrected for attenuation by soot between the LII image plane and camera. This was readily performed using the original extinction data used to calculate the f_v levels presented in reference [20]. To convert the relative LII intensities to f_v , each LII radial profile was multiplied by a scaling factor which was determined by the ratio of the radially summed f_v levels from all three axial positions to the radially summed LII intensity from all three axial positions. As can be seen from Fig. 6, good agreement is observed between the LII measurements and those derived from extinction in μg where both the relative spatial variations and intensities are similar. While previous tests of LII have shown it to yield accurate relative measurements in 1-g by comparison with light extinction and gravimetric sampling, these results are the first tests validating LII as a diagnostic for f_v in μg .

Results: 1g/ μg Comparion

Figure 7 shows both natural flame and corresponding (simultaneous) LII images of laminar atmospheric pressure diffusion flames of the 50/50 acetylene/nitrogen mixture in both 1-g and μg . The volumetric flow rate was 70 sccm. Each LII image was obtained with a single laser shot, with the μg image obtained after approximately 1 second of flame development in low-gravity. In contrast to the closed-tipped 1-g flame, the flame in μg is open-tipped, emitting soot. As predicted in [25], soot volume fraction levels are increased in laminar μg diffusion flames compared to 1-g. This is seen qualitatively in Fig. 7 and quantitatively in the radial profiles of Fig. 6. The soot volume fraction in μg reflects a competition between flame temperature and residence time. Lower

flame temperatures result in decreased fuel pyrolysis rates in gas-jet diffusion flames [26]. Absence of buoyancy-induced convection however leads to extended time scales for fuel pyrolysis and soot inception/growth reactions in μg because only the transport processes of forced convection (initial fuel jet momentum) and diffusion are operative [2].

The emission of soot from the flame can be explained by reduced soot oxidation rates. Radiative cooling, enhanced by the soot buildup, lowers the flame temperature thus lowering the oxidation rate of soot [27]. A similar rationale has been applied to gas-jet flames past their laminar smoke point [28]. Soot oxidation is also restricted by lowered oxidizer entrainment in the absence of buoyancy-induced convection. With decreased oxidation, soot volume fraction levels will increase and thus further enhance radiative heat loss until fuel pyrolysis and soot growth rates are slowed by lowered temperatures. That these rates are decreased by lowered flame temperatures can be observed in Fig. 7. Along the axial streamline, soot inception in μg is significantly delayed relative to 1-g.

Ethane

To demonstrate the sensitivity of LII in μg , ethane was chosen to produce lower soot concentrations in μg based on its lower sooting tendency in 1-g [29]. Figure 8 shows LII images obtained from an ethane-air jet diffusion flame of ethane in 1-g and μg (obtained 1 s after drop initiation). Due to buoyancy-induced instabilities, the normal gravity flame frequently flickered, consequently a representative image was chosen. At any instance in normal gravity, however, buoyant acceleration of the hot combustion products with resulting air entrainment causes radial confinement of the flame [30]. Due to initially lower temperatures, soot inception initiates last along the axial streamline. Due to initially lower OH, O and O₂ levels compared to outer radial positions, soot oxidation also ends last along the axial streamline [31]. With buoyant acceleration

eliminated in μg , the initial divergence of the exiting fuel flow is clearly seen, the resulting flame shape being determined by a combination of initial flow momentum, flow deceleration and stoichiometric requirements. Despite the fuel abundance within the central core of the flame, a combination of insufficient fuel pyrolysis products and diminished temperatures relative to 1-g likely inhibit soot formation reactions along the axial streamline resulting in the absence of soot at the flame tip.

Although the flicker observed in 1-g causes variation in peak f_v (for this flame roughly ranging from 0.2 to 0.4 ppm in the tip of the flame), f_v in μg increases to approximately 1 ppm based on a comparison of LII intensities. This example also illustrates the sensitivity of LII as the radially integrated f_v - pathlength product through the flame centerline is 6.7×10^{-7} cm yielding a transmittance of 0.95 using $K_e = 4.9$ based on the soot refractive index reported by Dazell and Sarofim [32] at 632.8 nm. Such a high transmittance is marginally detectable using unmodulated direct absorption methods and 8-bit digitization. On the basis of the camera gain calibration curve, approximately a factor of 30 higher sensitivity (or a factor of 30 lower f_v in μg) is achievable using a camera gain of 4.40 compared to 4.575 as was presently used. Such a high transmittance is likely undetectable even using sensitive lock-in detection of absorbance which possesses a practical limit of roughly 0.1 % absorbance sensitivity with RC time constants on the order of 100s of msec.

Propane

As a fuel with different soot concentration and stoichiometric requirements, propane was chosen. Figure 9 shows LII images of a gas-jet flame of propane in a) normal gravity and b) low gravity. Similar to the ethane flame in 1-g, the propane jet flame also flickered. Based on the LII intensity, camera gain and the camera calibration curve of Fig. 5, peak f_v s of approximately 4 and

8 ppm (in the annular region at mid-height) are measured for the flames in 1-g and μg (after approximately 1 sec into low-gravity) respectively, significantly higher than the f_v observed in the ethane gas-jet flame.

The larger spatial extent of the propane flame relative to the ethane flame for identical volume rates likely reflects the differing stoichiometry of the reaction. Increased oxidizer requirements result in increased flame surface area for a diffusion-limited transport process [33]. The soot inception/growth regions are also highly extended relative to those for ethane. Fuel molecular structure has been reported to affect soot growth processes and final soot volume fraction only at the earliest stages of soot formation [34-36]. Fuel pyrolysis products are the reactants available for the formation of PAHs, species directly responsible for soot inception and subsequent growth [37]. With a key intermediate step towards soot being formation of the first aromatic ring, propane can readily provide the C3 species required for benzene formation [38].

Vortex visualization

Visualization of a transient vortex and resolution of the steep spatial gradients requires the temporal and spatial capabilities of LII. Figure 10a is a LII image of soot within a vortex formed by a nonbuoyant propane flame issuing from a gas-jet nozzle while Fig. 10b is a contour plot of Fig. 10a. Initiation of fuel flow and subsequent ignition were performed in low-gravity. Based on the relative pixel intensities and camera gain calibration curve, absolute f_v s were assigned to the intensity contours derived from Fig. 10a. The central bulge is due to the initial jet momentum while the side recirculation regions result from air entrainment into the shear layer. The higher f_v in the recirculation regions is sensible as fuel parcels in these regions experience extended times at elevated temperatures promoting pyrolysis processes and soot growth.

Turbulent gas-jet flame

Soot volume fraction determination in a turbulent gas-jet diffusion flame is perhaps the best illustration of the combined spatial temporal capabilities of LII and its geometric versatility. Even using a detection gate of 500 ns, temporal frequencies of greater than 1 MHz can be frozen. As determined using a replicate of the 1951 Air Force test pattern, the spatial resolution is approximately 5 line pairs per millimeter allowing spatial structures of 0.1 mm to be resolved. Fig. 11 shows LII images from the turbulent gas-jet flame in 1-g and μg . The images are temporally uncorrelated and were chosen as representative of those obtained in each gravity environment. The images reveal a lower f_v level in the turbulent flame in μg with the soot containing regions less frequent and spatially disconnected compared to μg .

Insight into the f_v distribution can be achieved through histogram analysis of the f_v distribution. In both 1-g and μg , an image series consisting of 60 full-field LII images of the turbulent flame were obtained representing 2 seconds of continuous data. From each image in the series, a histogram can be calculated representing the number of pixels as a function of the digitized LII intensity (0-255). The histograms from each image in the LII 1-g and μg series were linearly averaged together. Using the camera gain calibration curve (Fig. 5) together with the signal level from the 50/50 acetylene/nitrogen mixture, the digitized LII intensity can be converted to absolute f_v . Using the image magnification the number of pixels can be converted to physical spatial extent. To accurately calculate the f_v histogram from LII images, the pixel (spatial element) resolution must be higher than spatial gradients in f_v to prevent spatial averaging. Visual inspection of the pixel intensities suggested this was so. As a check, similar individual image histogram intensity distributions were also obtained after selected images had been smoothed using an equal weight averaging filter using the 8 nearest neighbor pixel values.

Fig. 12 plots these averaged and converted histograms representing the spatial extent of f_v levels in 1-g and μg oxidation region of the turbulent flame. As suggested by the images and conveyed through the statistics, for any f_v level, the spatial region containing that f_v level is smaller in μg , particularly at high f_v levels. Moreover, based on Fig. 12, the spatial extent of soot containing regions is smaller, thus the spatially averaged f_v level in μg is also lower than in 1-g. These results are somewhat counterintuitive because the absence of buoyant air-entrainment and slower removal rate of hot combustion products would be expected to lead to an increase in f_v . Further investigation is underway.

Conclusions

The sensitivity, temporal and spatial capabilities in addition to geometric versatility enable LII as a laser-based planar imaging technique to determine the soot spatial distribution and concentration in laminar and turbulent studies. These capabilities are particularly useful in comparing combustion processes in microgravity and normal gravity. With the elimination of buoyancy-induced convection, both flame shape and f_v differ substantially compared to the same fuel/burner system in normal gravity. Spatial and concentration differences of f_v in 1-g and μg environments are readily illustrated by comparison of the LII images. Validation of LII for f_v determination in μg was demonstrated by comparison of LII radial intensity profiles with radial f_v s derived via extinction for a laminar gas-jet flame of acetylene/nitrogen in μg . Application of LII to laminar gas-jet diffusion flames of ethane, propane, an acetylene/nitrogen mixture, a transient vortex flame of propane and a turbulent diffusion flame of acetylene in low-gravity demonstrate the advantages and capabilities of LII for absolute f_v determination.

Acknowledgements

This work was supported through NASA contract, NAS3-27186. The author thanks Prof. J. C. Ku (Wayne State University) and P. S. Greenberg (NASA-Lewis) for sharing their full-field light extinction data.

Disclaimer

Manufacturer and product names are used to aid understanding and do not constitute an endorsement by either Nyma Inc. or the federal government.

References

1. Soot Formation in Combustion. (H. Bockhorn Ed.), Springer-Verlag, Heidelberg, (1994).
2. Mortazavi, S., Sunderland, P. B., Jurng, J., Koylu, U. O. And Faeth, G. M., Structure of soot-containing laminar jet diffusion flames. AIAA paper 93-708 (1993).
3. Faeth, G. M., Laminar jet diffusion flames in microgravity: A paradigm for soot processes in turbulent flames. Sciences Requirement Document, NASA-Lewis, 1992.
4. Law, C. K. And Faeth, G. M., Opportunities and challenges in microgravity combustion. Prog. Energy Combust. Sci. 20:65 (1994).
5. Ku, J. C. And Tong, L., Detailed modeling analysis for soot formation and radiation in microgravity gas jet diffusion flames. Proceedings of the Third International Microgravity Combustion Workshop, (NASA Conference Publication 10174), April 11-13, Cleveland, OH, p. 375 (1995).
6. Atreya, A., Agrawal, S., Shamim, T., Pickett, K. And Sacksteder, K. R., Radiant extinction of gaseous diffusion flames. Proceedings of the Third International Microgravity Combustion Workshop, (NASA Conference Publication 10174), April 11-13, Cleveland, OH, p. 319 (1995).
7. Echigo, R., Nishiwaki, N. And Hirata, M., Radiation from nonhomogenous combustion products. The Eleventh Symposium on Combustion (International), The Combustion Institute, (1976) p. 381.
8. Dec, J. E., zur Loye, A. O. and Siebers, D. L., Soot distribution in a D. I. Diesel engine using 2-D Imaging of laser-induced incandescence, elastic scattering and flame luminosity. SAE Tech. Paper 910224 (Society of Automotive Engineers), Warrendale, PA, (1991).
9. Pinson, J. A., Mitchell, D. L., Santoro, R. J. and Litzinger, T. A., Quantitative planar soot measurements in a D.I. Diesel engine using laser-induced incandescence and light scattering. SAE Tech. Paper 932650 (Society of Automotive Engineers), Warrendale, PA, (1993).
10. Quay, B., Lee, T. W., Ni, T. and Santoro, R. J., Spatially resolved measurements of soot volume fraction using laser-induced incandescence. Combust. and Flame 97:394 (1994).
11. Vander Wal, R. L. and Weiland, K. J., Laser-induced incandescence: development and characterization towards measurement of soot volume fraction. J. Appl. Phys. B59:445 (1994).
12. Shaddix, C. E., Harrington, J. E. and Smyth, K. C., Quantitative measurements of enhanced soot production in a flickering methane air diffusion flame. Combust. and Flame 99:723 (1995).

13. Shaddix, C. R. and Smyth, K. C., Laser-induced incandescence measurements of soot production in steady and flickering methane, propane and ethylene diffusion flames. *Combust. and Flame* 107:418-452 (1996).
14. Ni, T., Pinson, J. A., Gupta, S. and Santoro, R. J., Two-dimensional imaging of soot volume fraction by the use of laser-induced incandescence. *Appl. Opt.* 34:7083 (1995).
15. Vander Wal, R. L., Jensen, K. A. and Choi, M. Y., Simultaneous laser-induced emission of soot and polycyclic aromatic hydrocarbons within a gas-jet diffusion flame. *Combust. and Flame* 109:399, (1997).
16. Vander Wal, R. L. Onset of carbonization: Spatial location via simultaneous LIF-LII and characterization via TEM. *Combust. Sci. and Technol.* 118:343-360 (1996).
17. Vander Wal, R. L., Zhou, Z. And Choi, M. Y., Laser-induced incandescence calibration via gravimetric sampling. *Combust. and Flame* 105:462 (1996).
18. Vander Wal, R. L. and Dietrich, D. L., Laser-induced incandescence applied to droplet combustion. *Appl. Opt.* 34:1103 (1995).
19. Ku, J. C., Griffin, D. W., Greenberg, P. S. And Roma, J., Buoyancy-induced differences in soot morphology. *Combust. And Flame* 102:216 (1995).
20. Greenberg, P. S. and Ku, J. C., Soot volume fraction maps for normal and reduced gravity laminar acetylene jet diffusion flames. *Combust. And Flame* 108:227 (1997).
21. Lekan, J., Gotti, D. J., Jenkins, A. J., Owens, J. C. and Johnston, M. R., A drop-tower user's guide. NASA Technical Memorandum 107090, April, (1996).
22. The turbulent burner was designed by P. S. Greenberg (NASA-Lewis).
23. Stanford Research Systems, Application Notes, Note no. 4, p.186 (1996-1997).
24. Engstrom, R. W., RCA Photomultiplier handbook, The RCA Corporation (1980).
25. Bahadori, M. Y., Edelman, R. B., Stocker, D. P. And Olson, S. L., Ignition and behavior of laminar gas-jet diffusion flames in microgravity. *AIAA J.* 28:236 (1988).
26. Leung, K. M., Lindstedt, R. P. and Jones, W. P., A simplified reaction mechanism for soot formation in nonpremixed flames. *Combust. and Flame* 87:289 (1991).

27. Kent, J. H. And Wagner, H. GG., Temperature and fuel effects in sooting diffusion flames. Twentieth Symposium (International) on Combustion, The Combustion Institute, Pittsburgh, PA, p. 1007 (1984).
28. Kent, J. H. And Wagner, H. GG., Why do diffusion flames emit smoke? *Combust. Sci. And Technol.* 41:245 (1984).
29. Schug, K. P., Manheimer-Tinmat, Y., Yaccarino, P. And Glassman, I., Sooting behavior of gaseous hydrocarbon diffusion flames and the influence of additives. *Combust. Sci. And Technol.* 22: 235 (1980).
30. Sunderland, P. B., Mortazavi, S. Faeth, G. M. and Urban, D., Laminar smoke points of nonbuoyant jet diffusion flames. *Combust. And Flame* 96:97 (1994).
31. Puri, R., Santoro, R. J. And Smyth, K. C., The oxidation of soot and carbon monoxide in hydrocarbon diffusion flames. *Combust. And Flame* 97: 125 (1994).
32. Dalzell, W. H. and Sarofim, A. L. Optical constants of soot and their application to heat-flux calculations. *J. Heat Transfer* 91:100 (1969).
33. Edelman, R. B. and Bahadori, M. Y., Effects of buoyancy on gas-jet diffusion flames: experiment and theory. *Acta Astronautica* 13:681 (1986).
34. Gomez, A., Sidebotham, G. and Glassman, I., Sooting Behavior in temperature-controlled laminar diffusion flames. *Combust. And Flame*, 58:45(1984).
35. Frenklach, M., Clary, D. W., Gardiner, W. C. and Stein, S. E., Effect of fuel structure on pathways to soot. The Twenty-First Symposium (International) on Combustion, The Combustion Institute, Pittsburg, PA pp. 1067 (1986).
36. Gulder, O. L., Influence of hydrocarbon fuel structural constitution and flame temperature on soot formation in laminar diffusion flames . *Combust. And Flame*, 78:179 (1989).
37. Frenklach, M. and Wang, H., Effect of fuel structure on pathways to soot. Twenty-Third Symposium (International) on Combustion, The Combustion Institute, Pittsburgh, PA, pp. 1559 (1990).
38. Leung, K. M. and Lindstedt, R. P., Detailed kinetic modeling of C1-C3 alkane diffusion flames. *Combust. And Flame*, 102:129 (1995).

Figure Captions

Figure 1

Top view of the hardware and optical layout of the drop rig (a) and corresponding sideview (b).

Figure 2

Equipment and signals layout.

Figure 3

Laser and video timing.

Figure 4

Average LII pixel intensity versus neutral density filter value (ND) preceding the LII camera.

Figure 5

Camera intensifier gain calibration curve. Note that higher intensifier gain settings correspond to lower readout voltage settings. See text for details.

Figure 6

Radial intensity profiles for a 50/50 acetylene/nitrogen (volume/volume) laminar gas-jet flame in both 1-g and μg . Comparison is made between the LII signal intensity and f_v values derived from a full-field light extinction method discussed elsewhere (ref. 20). See text for details.

Figure 7

Natural flame luminosity and corresponding (simultaneous) LII images of a laminar 50/50 acetylene/nitrogen (volume/volume) flame in both 1-g and μg obtained with a single laser shot.

The images represent the flame after a time duration in low-gravity of approximately 1 second. The burner nozzle is 1 mm above the picture bottom but is not visible in the LII image. The ruler spatial scale is in millimeters.

Figure 8

LII images of a laminar ethane diffusion flame in 1-g and μg . The burner nozzle is 11 mm below the Fig. bottom. The ruler spatial scale is in millimeters.

Figure 9

LII images of a laminar propane diffusion flame in 1-g and μg . The burner nozzle is 11 mm below the Fig. bottom. The ruler spatial scale is in millimeters.

Figure 10

a.) LII image of a vortex formed during initial formation of a laminar gas-jet flame of propane in μg . b.) Contour plot of (a) with f_v values given in ppm. Both fuel flow and ignition were initiated in μg . The nominal steady-state Reynolds number of 330. The burner nozzle is 11 mm below the picture bottom. The ruler spatial scale is in millimeters.

Figure 11

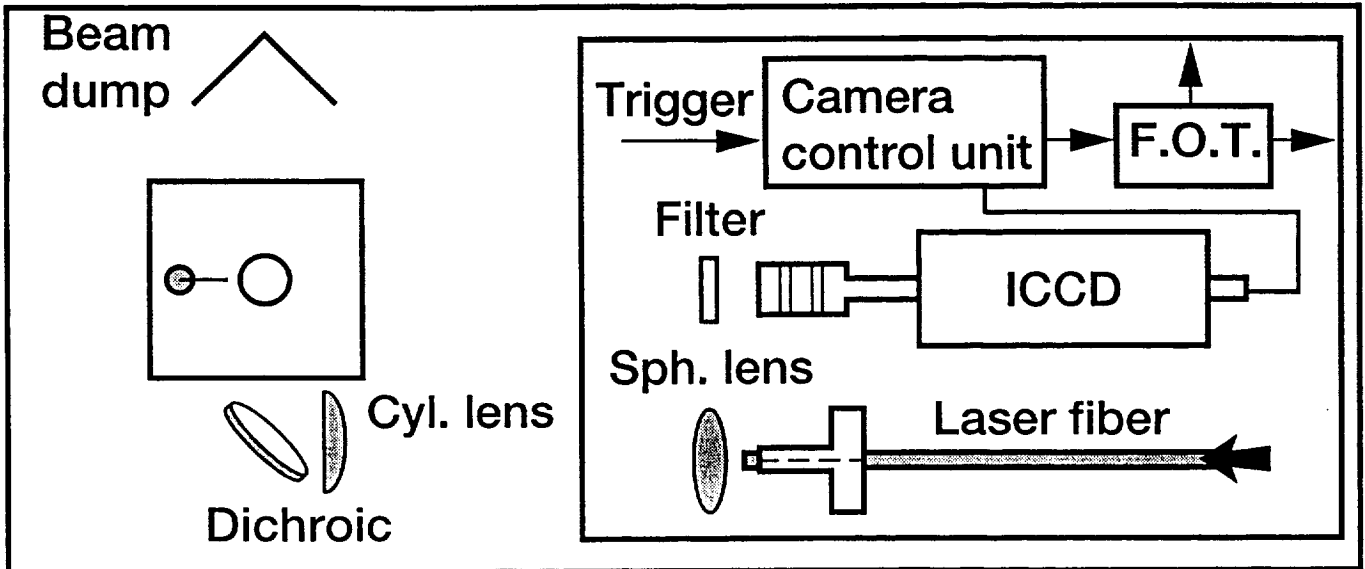
LII images of soot within the oxidation region of a turbulent gas-jet flame of acetylene in 1-g and μg . The image bottom is 110 mm above the burner nozzle. The ruler spatial scale is in millimeters.

Fig. 12

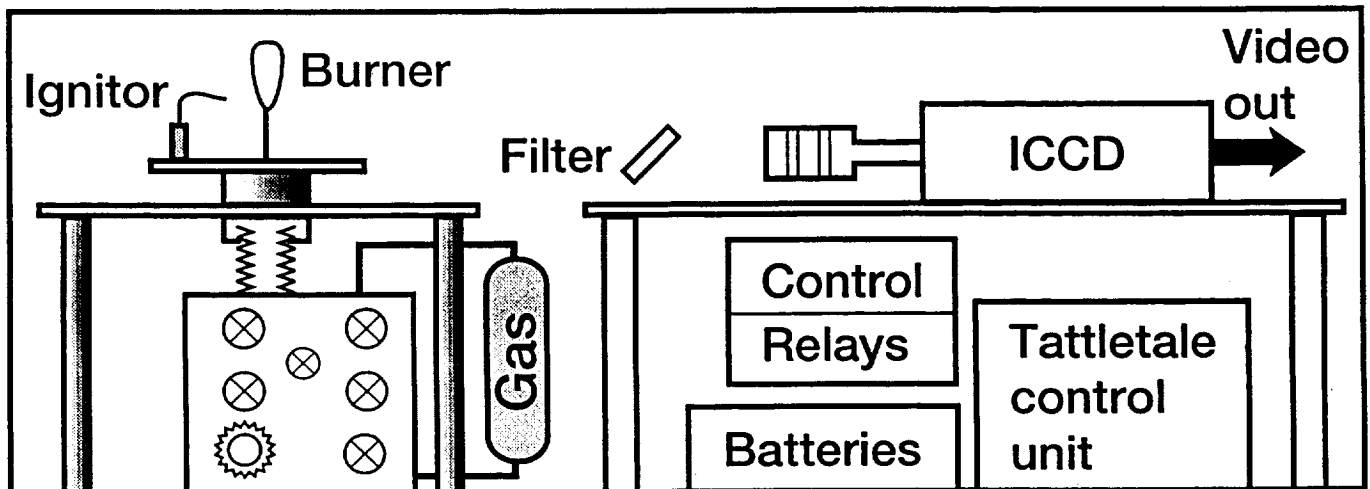
Histograms of the spatial extent of different f_v levels (binning category). The histograms were calculated from series of LII images in 1-g and μg with quantification of f_v levels and spatial extent as described in the text.

Drop Rig Schematic

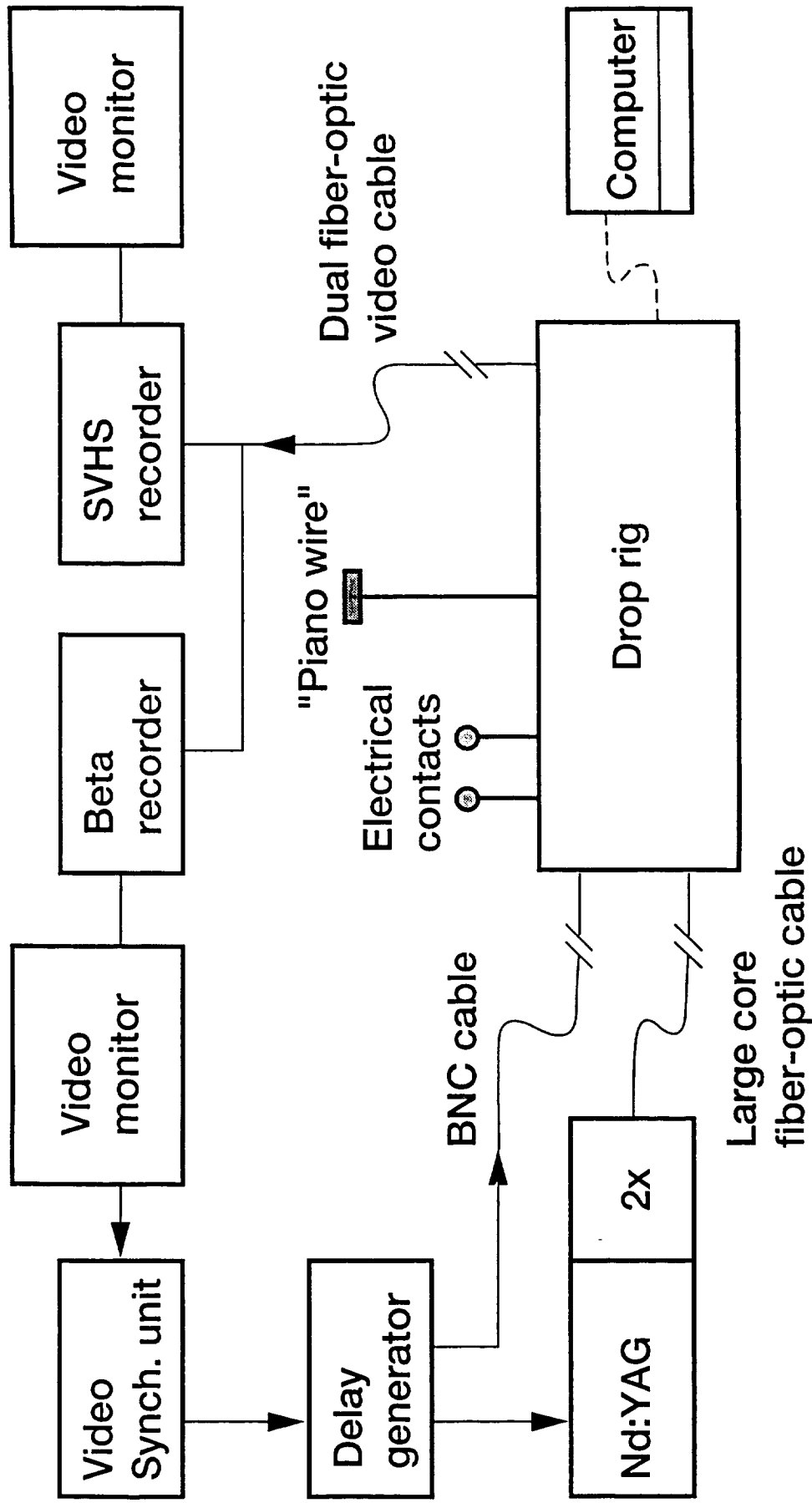
Top View



Side View

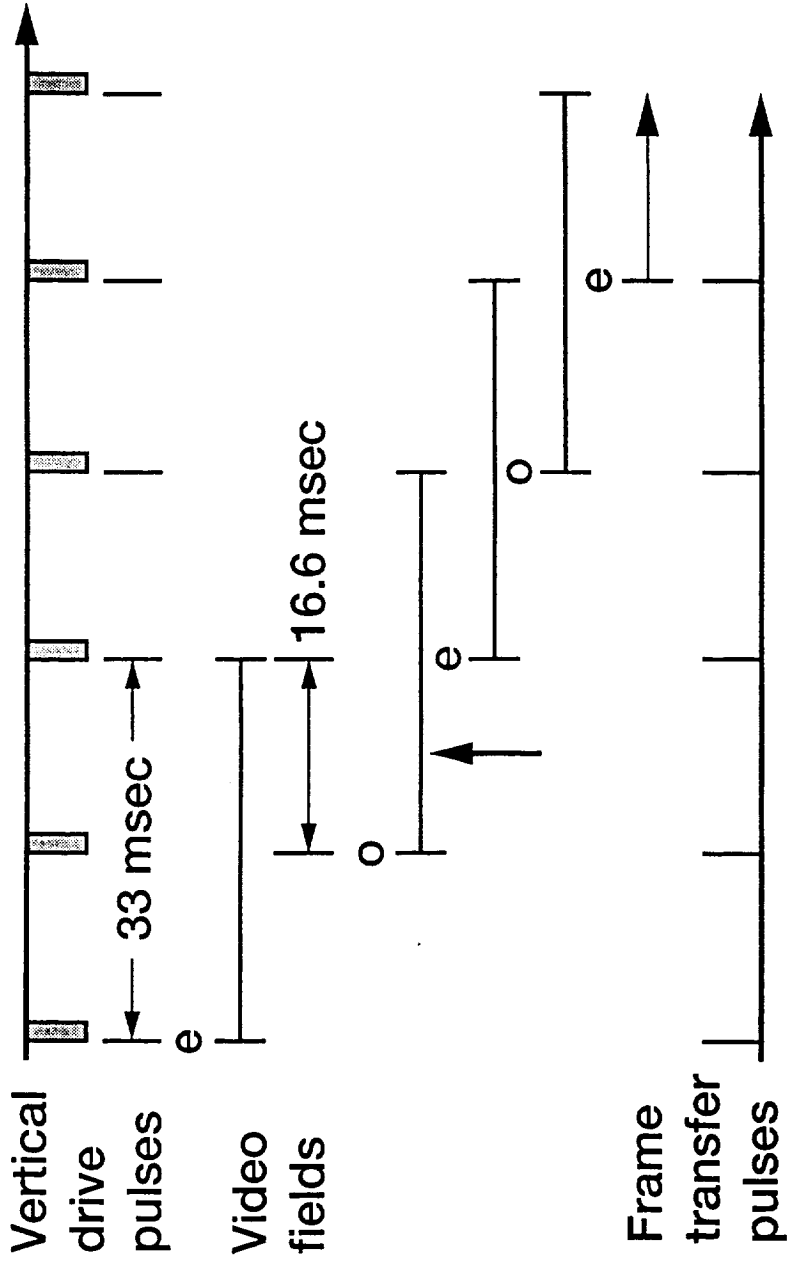


Experimental Schematic

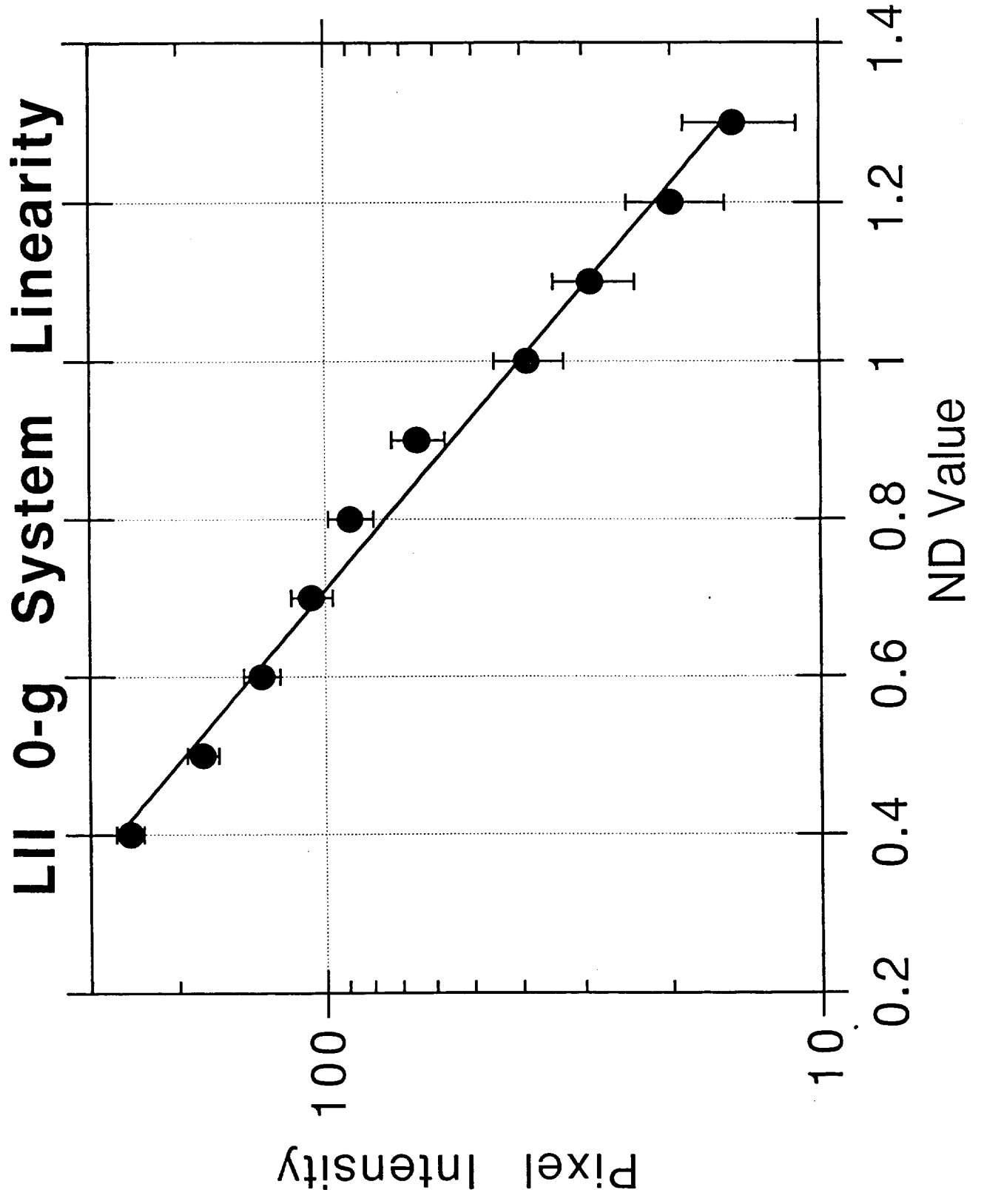


CD-97-74324

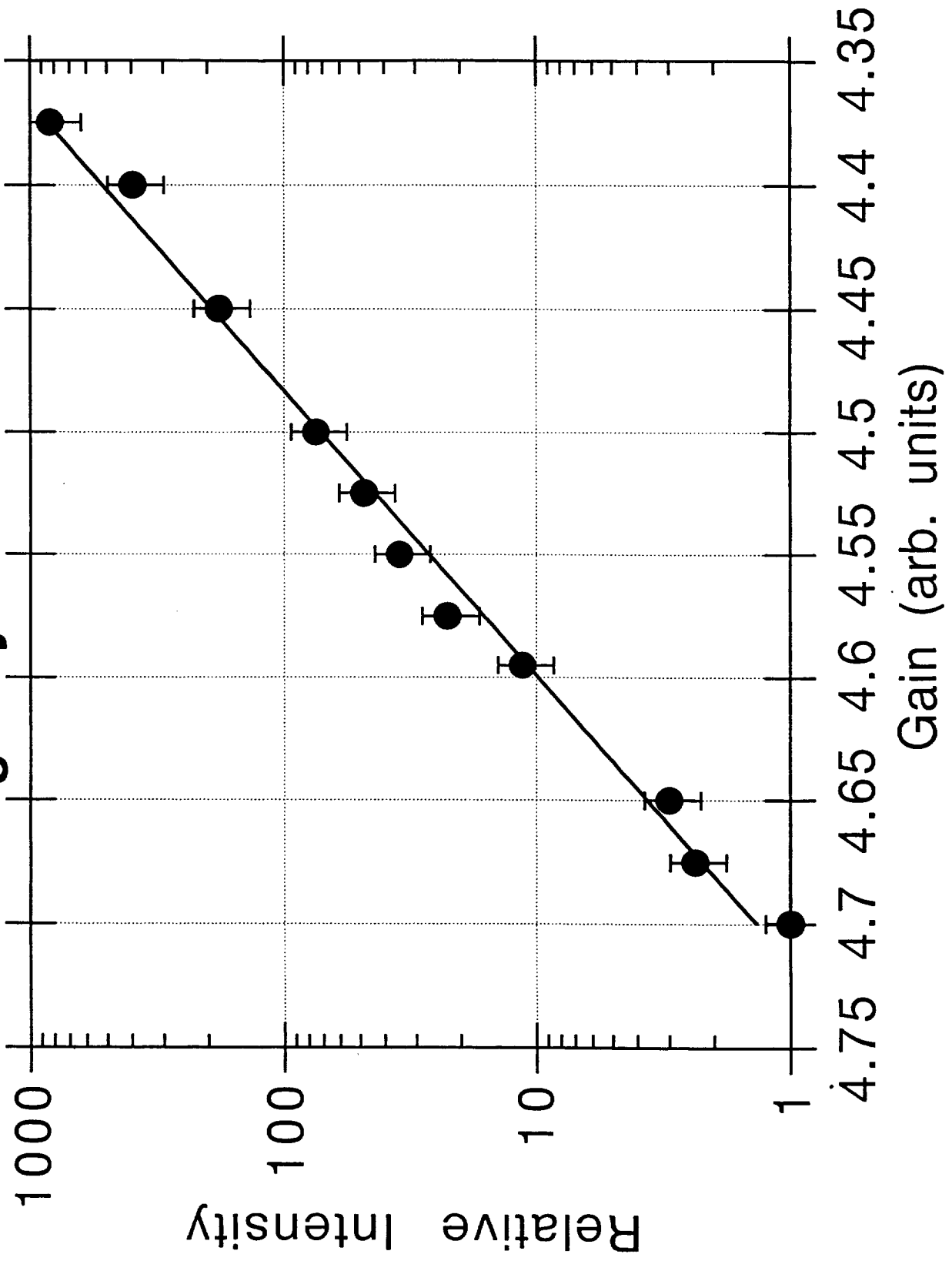
Video Timing



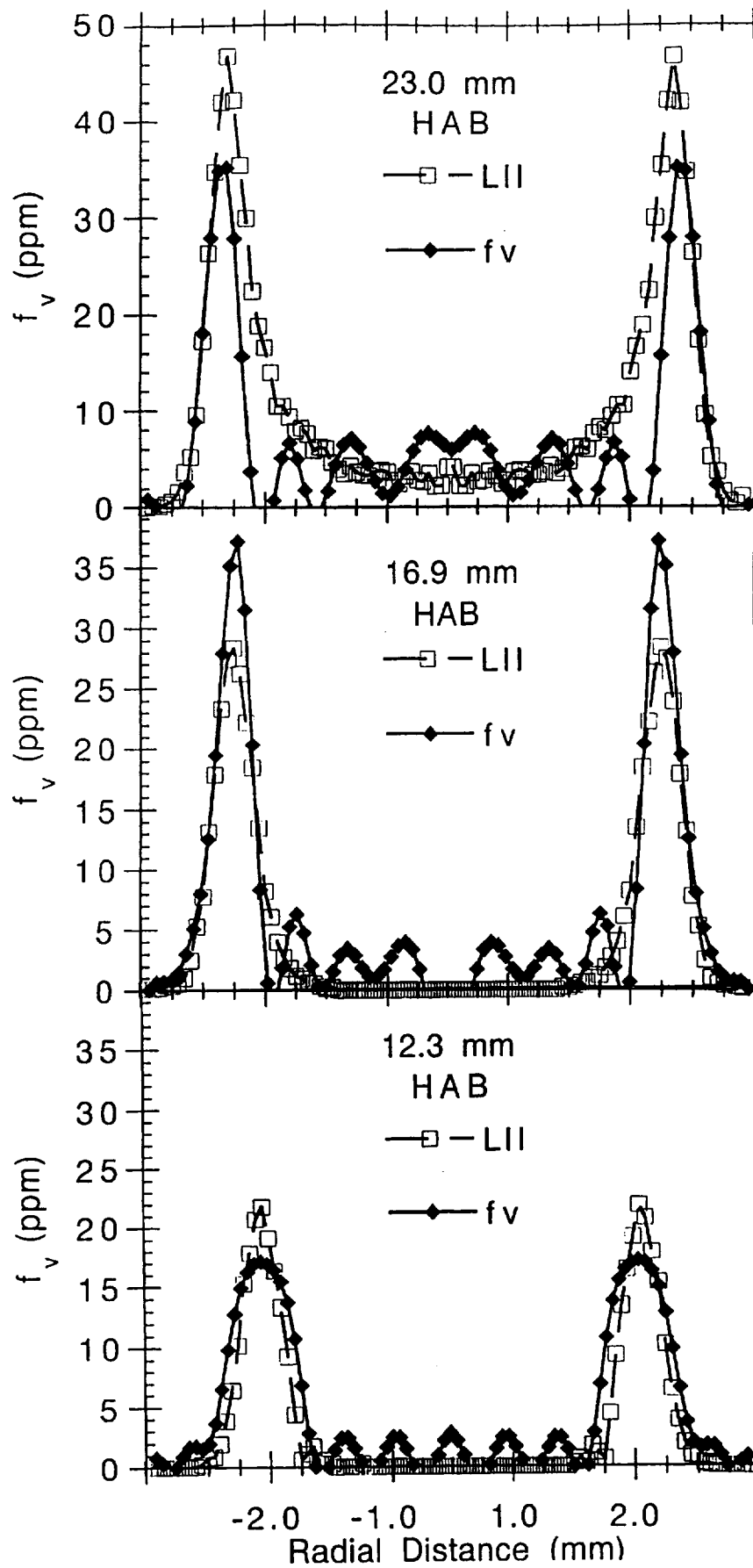
CD-97-74326



LII 0-g System Calibration



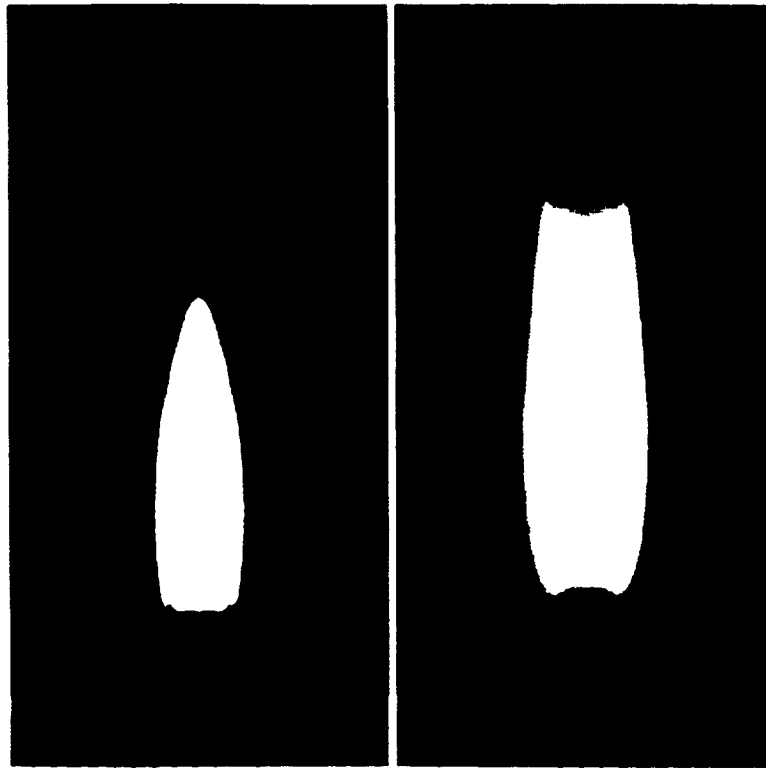
5



Natural Flame Images

1g

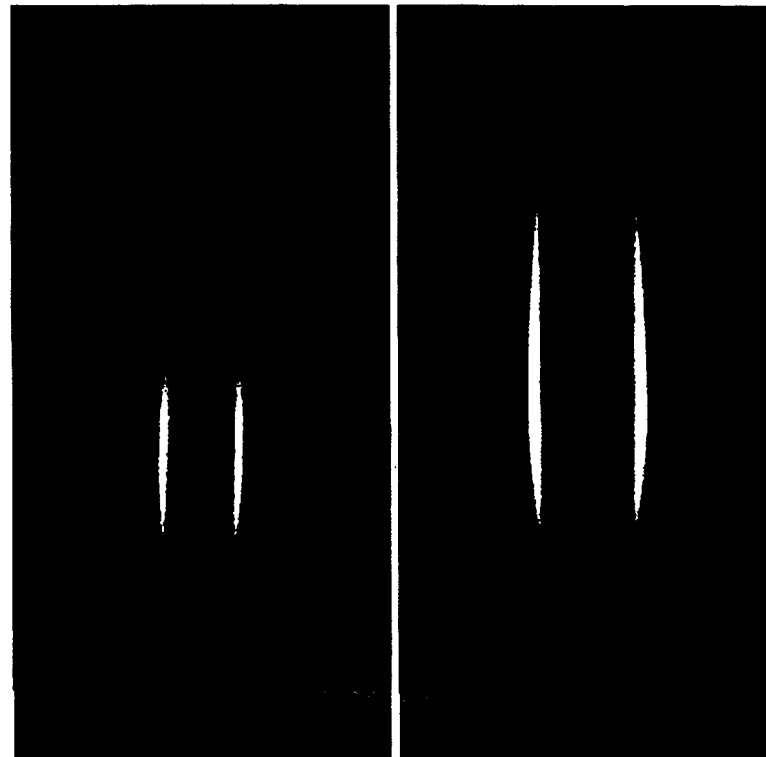
0g

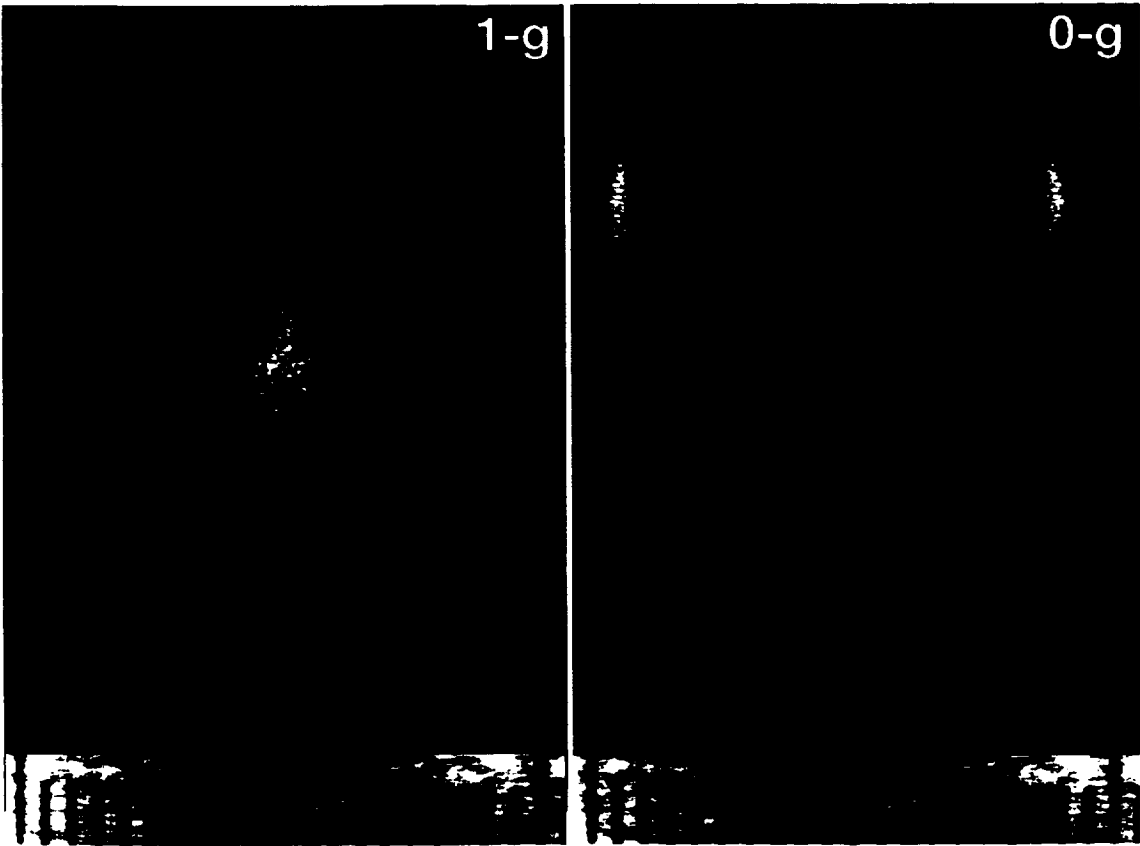


1g

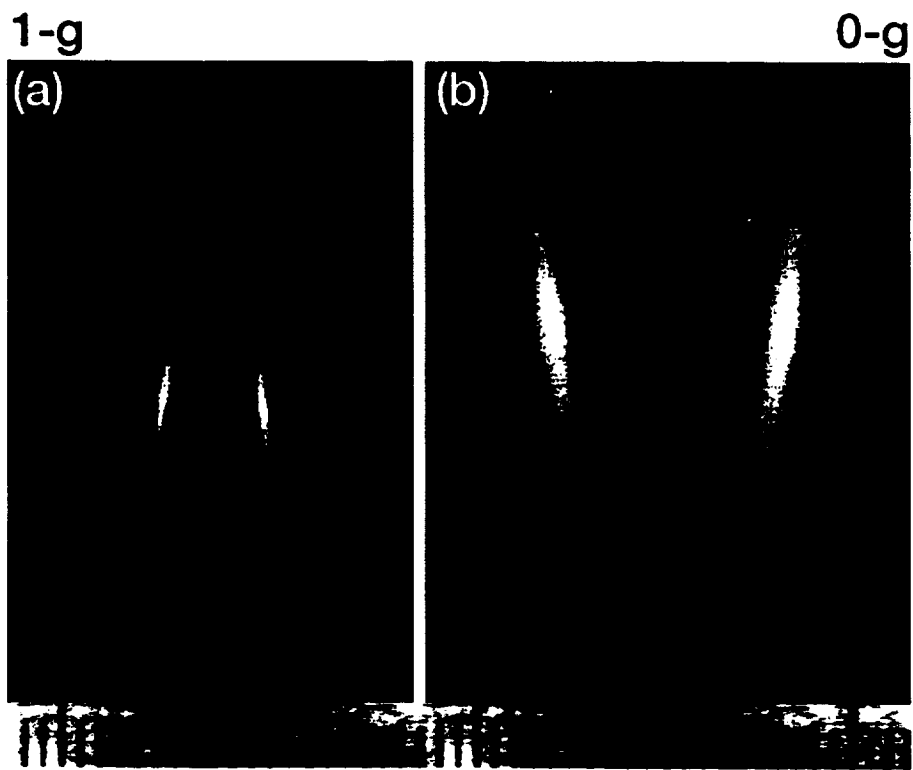
LII Images

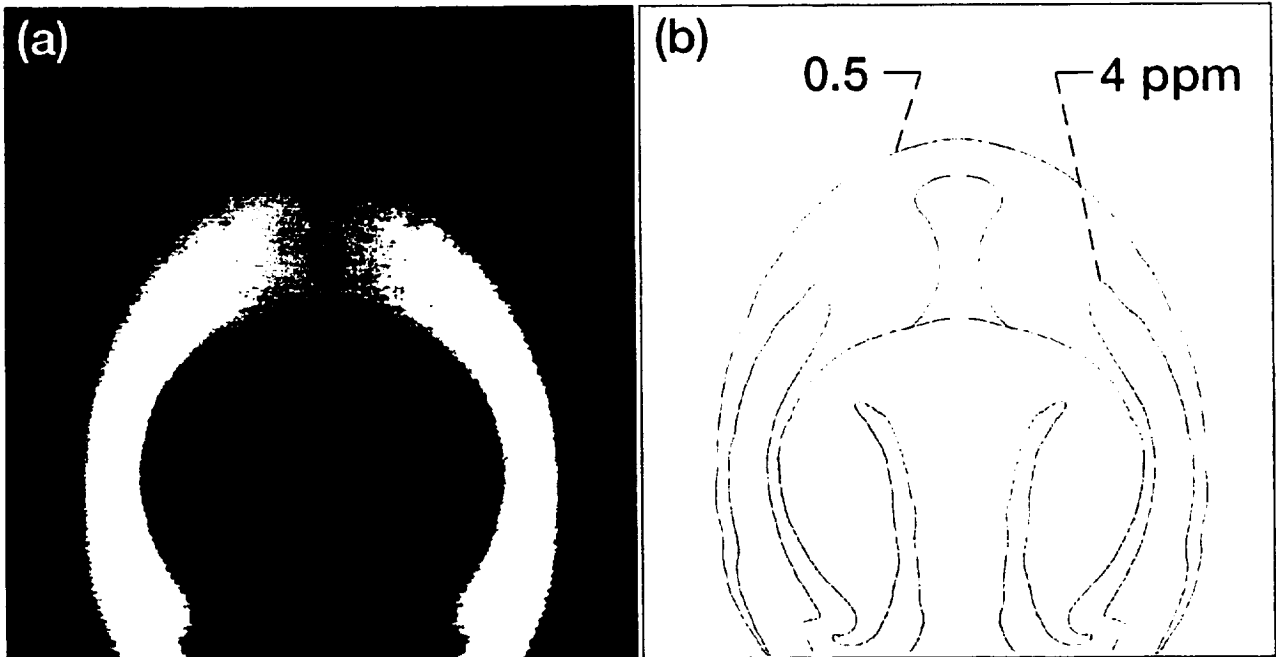
0g

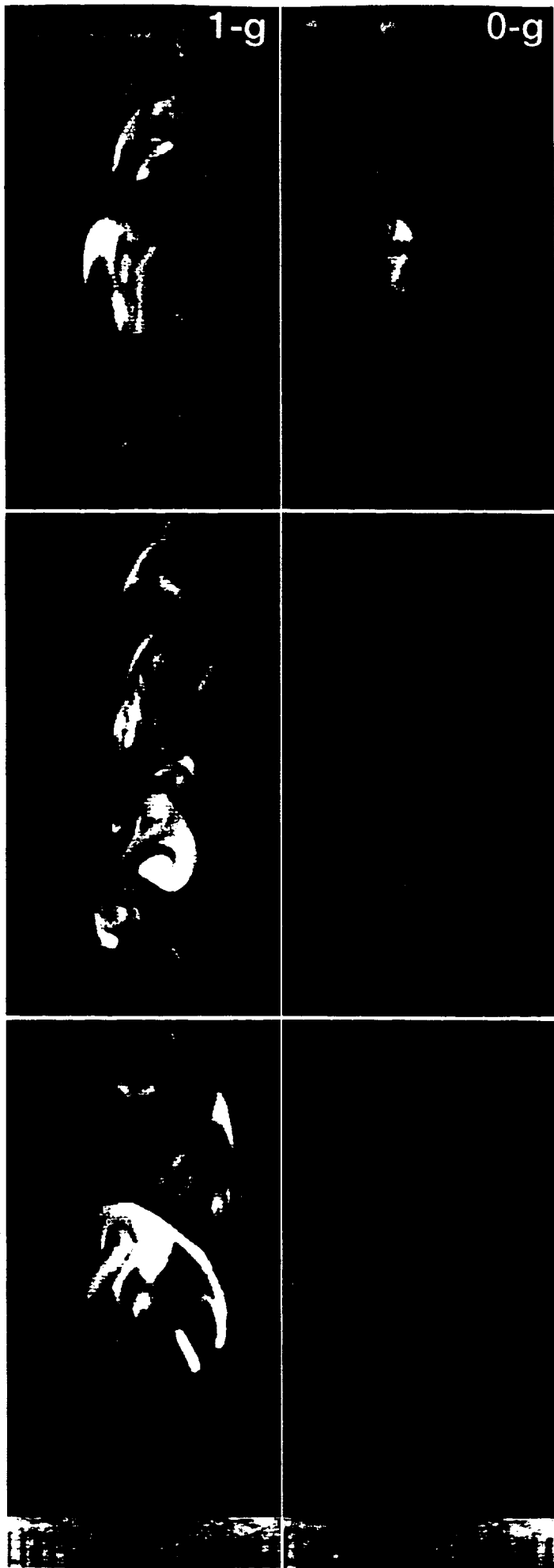




CD-97-74550







11

